ELSEVIER

Contents lists available at ScienceDirect

Journal of Materials Research and Technology

journal homepage: www.elsevier.com/locate/jmrt





Effect of secondary phases on electrical conductivity and thermal conductivity of HPDC Al-Ni and Al-Fe alloys: A comparative study

Hongbin Xing ^a, Fanjin Yao ^a, Qianxi Zhang ^a, Bo Hu ^{a,*}, Minke Qian ^b, Jun Jiang ^c, Bensong Chen ^d, Wanzhang Yang ^d, Dejiang Li ^{a,**}, Xiaoqin Zeng ^a

- ^a National Engineering Research Center of Light Alloy Net Forming & State Key Laboratory of Metal Matrix Composites, School of Materials Science and Engineering, Shanghai Jiao Tong University, Shanghai, China
- Suzhou Huijin Smart Materials Technology Co., Ltd, China
- ^c Yunnan Yunlv Runxin Aluminum Industry Co., Ltd., Honghe, 651400, China
- d Yunnan Aluminium Co., Ltd., Kunming, 650500, China

ARTICLE INFO

Handling Editor: L Murr

Keywords: Aluminum alloys Electrical property Thermal conductivity Secondary phases

ABSTRACT

Solute atoms and secondary phases are the principal determinants of the electrical and thermal conductivity of aluminum (Al) alloys. However, the influence of secondary phases has often been undervalued compared to that of solute atoms. Herein, Al-Ni and Al-Fe alloys with gradient alloying contents were fabricated via high-pressure die casting (HPDC) to comparatively scrutinize the influence of the microscopic secondary phases on the macroscopic electrical and thermal conductivity of Al alloys. The results demonstrated that the microscopic conductive properties, morphology, and volume fraction of the secondary phases were the predominant factors influencing the electrical and thermal conductivity of Al alloys. Correspondingly, Al-Ni alloys demonstrated improved electrical and thermal conductivity, primarily due to the favorable microscopic electrical and thermal conductivity of their secondary phases, the elimination of morphology-induced electron scattering from needle-like secondary phases, and their comparatively lower secondary phase volume fractions. This research deepens the understanding of the microscopic secondary phase on macroscopic electrical conductivity and thermal conductivity of Al alloys, thereby contributing to the development of advanced Al alloys with enhanced conductive properties.

1. Introduction

With the increasing urgency of addressing environmental and energy challenges, new energy vehicles have witnessed rapid growth driven by technological advances and market demand, and are expected to occupy a more prominent position in future transportation systems [1]. As the core component of the new energy vehicles, traction motors are mainly categorized into permanent magnet synchronous motors and asynchronous motors. The permanent magnet synchronous motors are constrained by high costs, limited power range, and complex control systems. In contrast, the asynchronous motors offer advantages such as reduced cost, an extensive power output range, compact structural configuration, and convenient maintenance, thereby demonstrating greater compatibility with the evolving technological and industrial requirements of new energy vehicle development [2].

Al alloys have emerged as critical materials in the new energy vehicle industry, attributed to their low density, high specific strength, excellent electrical/thermal conductivity, superior castability, distinctive corrosion resistance, and considerable recycling potential [3–5]. These attributes collectively contribute to improved economic efficiency, structural-functional performance, and resource sustainability in automotive manufacturing [6]. At present, pure Al and Al alloys are predominantly employed as the rotor material in asynchronous motors [2]. Nonetheless, two major limitations hinder their broader application: (i) the intrinsic trade-off between electrical conductivity and strength [7–9], and (ii) strength degradation induced by thermal accumulation during service operation [10,11].

Although pure Al possesses a relatively high electrical conductivity (\sim 35 MS/m) that meets the requirements for motor rotors (>27 MS/m), its low tensile strength (<100 MPa) compromises the safety and

E-mail addresses: 1969220462@sjtu.edu.cn (B. Hu), lidejiang@sjtu.edu.cn (D. Li).

https://doi.org/10.1016/j.jmrt.2025.09.178

^{*} Corresponding author.

^{**} Corresponding author.

reliability under high-speed operating conditions [12,13]. In contrast, conventional commercial Al alloys offer improved strength but suffer from reduced electrical conductivity, leading to increased energy losses decreased operational efficiency [14,15]. Hence, conductivity-strength trade-off has emerged as a fundamental scientific bottleneck hindering the development of Al alloys for motor rotor applications [16–18]. This trade-off originates from the inherently conflicting nature of metallic materials [19]. The electric conduction of metallic materials primarily relies on the directional movement of free electrons, and the electrical conductivity is directly proportional to the mean free path of the electrons [20]. When alloying elements are present in solute atoms, they introduce significant lattice distortions in the Al matrix, thereby substantially reducing the electron mean free path and leading to a marked decline in electrical conductivity. Moreover, secondary phases act as supplementary scattering centers for electron transport [21]. Therefore, alloying generally results in a degradation of the electrical conductivity of Al alloys [22]. Fortunately, the detrimental effect of alloying elements on electrical conductivity is markedly mitigated when these elements are primarily present as secondary phases instead of solute atoms [23]. Furthermore, secondary phase strengthening represents one of the most effective mechanisms for enhancing the mechanical properties of Al alloys [24]. Therefore, alloying elements with negligible solubility in Al, which readily form secondary phases, offer a pragmatic compromise for enhancing strength while retaining the high electrical conductivity. Notably, both Ni and Fe are representative alloying elements with low solubility in Al matrix (0.19 and 0.02 at. % at eutectic temperature, respectively [25]), which qualifies them as ideal candidates for the design of high-conductivity, high-strength Al alloys. A comparative study between these two systems helps elucidate the distinct influences of intrinsic properties and morphology of the secondary phases on conductive and mechanical properties. Previous studies have demonstrated that Al-Ni and Al-Fe alloys demonstrate superior electrical conductivity compared to conventional systems such as Al-Si, Al-Cu, and Al-Mg alloys [26]. These results indicated that Ni and Fe exerted relatively limited detrimental effects on electrical conductivity, thereby underscoring their viability as pivotal alloying elements in the development of advanced high-conductivity Al alloys [25]. Correspondingly, Zhang et al. [16] proposed a high-conductivity Al-2Fe-1Ni alloy designed with the volume fraction and morphology of intermetallic compounds. The fibrous, rod-like morphology of the secondary phases contributed to suppressing electron scattering and preserving conduction pathways by providing more space for electron movement [27].

Furthermore, motor rotors unavoidably experience heat accumulation during operation, resulting in elevated service temperatures that subsequently lead to strength degradation. Improving the thermal conductivity of Al alloys for motor rotors is therefore essential for enhancing thermal management capabilities and delaying thermally induced strength deterioration [27]. In metallic systems, electrons serve as the primary carriers of thermal energy [28,29]. According to the Wiedemann-Franz law [22], the electrical conductivity of most metals is generally proportional to their thermal conductivity at a given temperature (excluding extremely high- or low-temperature conditions). Consequently, strategies that enhance electrical conductivity are simultaneously beneficial to thermal conductivity. Alloying elements with low solid solubility in Al matrix (such as Ni and Fe) tend to form secondary phases, which facilitate improvements in both electrical and thermal conductivity of Al alloys while suppressing the degradation of strength under thermal exposure [30]. Despite advancements in high-conductivity Al alloy research, the effects of microscopic intrinsic properties and morphology of the secondary phases on the macroscopic electrical conductivity and thermal conductivity of Al-Ni and Al-Fe allovs remain insufficiently understood.

In this study, Al-Ni and Al-Fe alloys were employed as comparative systems to investigate the influence of secondary phases on the electrical and heat conduction behavior of Al alloys. The microstructure of the

diverse Al-Fe and Al-Ni alloys was scrutinized. The evolutions of the electrical conductivity, thermal conductivity, and mechanical properties of the Al-Ni and Al-Fe alloys with the diverse alloying contents were investigated. The microscopic electric conduction behaviors based on different secondary phases in diverse Al-Ni and Al-Fe alloys was comprehensively characterized and quantitatively compared. The heat conduction behavior was investigated using diverse theoretical heat conduction models and finite-element simulations based on actual microstructure features. This study enhances the understanding of how microscopic secondary phases affect the macroscopic electrical and thermal conduction properties of HPDC Al alloys, thereby offering a technical foundation for the design of high-performance Al alloys for asynchronous motor rotor applications.

2. Experimental details

2.1. Specimen preparation

The asynchronous motors are typically manufactured using high-pressure die casting (HPDC) due to its high efficiency, high dimensional accuracy, and capability to produce complex, thin-walled components in a single molding step [31–33]. Informed by the differences in eutectic points of the Al-Ni and Al-Fe phase diagrams, the representative Al-xNi (x = 0.5, 1.0, 1.5, 2.0, 3.0, and 4.0 (wt. %)) and Al-xFe (x = 0.5, 1.0, 1.5, and 2.0 (wt. %)) alloys were prepared utilizing a horizontal cold chamber die casting apparatus with a clamping force of 3500 kN (TOYO/BD-350V5). The chemical composition of these alloys was analyzed using the inductively coupled plasma analyzer (ICP-OES, PERKINE 7300DV). The compositional analysis results are summarized in Table 1. A schematic depiction of the die-casting configuration and the associated process parameters are shown in Fig. 1 and Table 2, respectively.

2.2. Characterization

The microstructures of the diverse Al-Fe and Al-Ni alloys were characterized using a field-emission scanning electron microscope (FE-SEM, Carl Zeiss Sigma 560) equipped with energy-dispersive X-ray spectroscopy (EDX). The Phase identification was performed by X-ray diffraction (XRD, Rigaku MiniFlex 600) employing Cu- K_{α} ($\lambda = 1.54056$ Å) radiation at a scan rate of 1°/min. The concentrations of solute atoms were quantified by averaging at least five EDX measurements randomly selected from the Al matrix regions. The electrical conductivity was evaluated utilizing an eddy current conductivity meter (Sigma 2008B). The thermal diffusivity (α) was examined at room temperature (25 °C) using a laser flash apparatus (Netzsch LFA 467HT). The specific heat capacity (C_p) was determined by referencing standard samples (pure Cu, Φ 12.7 × 2.5 mm) within the same system. The density (ρ) was quantified via Archimedes principle (ET-320). Thermal conductivity (λ) at room temperature was subsequently calculated using the relation $\lambda =$ $\rho\alpha C_p$. All thermal property measurements were repeated at least three times to ensure reproducibility. The uniaxial tensile tests were conducted using a universal testing machine (Zwick Z100) on gauge specimens (Φ 6.4 × 55 mm) at a constant crosshead speed of 1.0 mm/min. Each test condition was replicated on a minimum of three specimens for statistical reliability. The Vickers hardness measurements were performed under a load of 500 g with a dwell time of 5 s. The microscopic

Table 1Quantitative chemical compositions of the Al-xFe and Al-xNi alloys determined by ICP-AES.

Ni nominal content (wt. %)	0.5	1.0	1.5	2.0	3.0	4.0
Ni actual content	0.48	0.99	1.53	2.01	3.07	4.11
Fe nominal content (wt. %)	0.5	1.0	1.5	2.0		
Fe actual content	0.52	1.00	1.46	1.96		

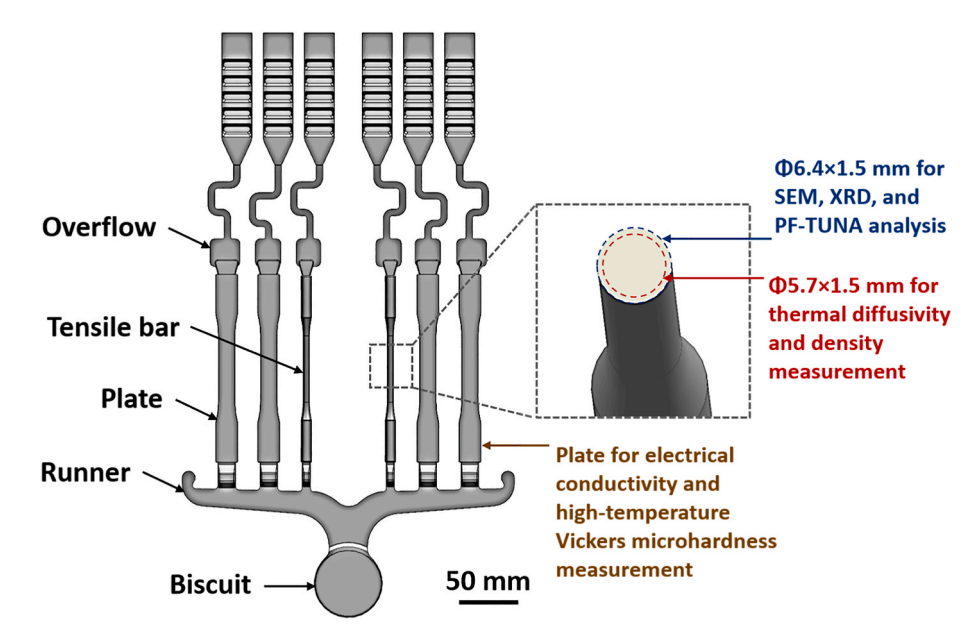


Fig. 1. Schematic of the die-casting configuration and specimen extraction.

Table 2
HPDC processing parameters used in this study.

Parameters	Melting temperature (°C)	Initial mold temperature (°C)	Slow-shot speed (m/s)	Fast-shot speed (m/s)	Intensification pressure (MPa)	Mold holding time (s)
Value	730	200	0.2	4.0	90	7

electric conduction behaviors of distinct secondary phases were quantitatively investigated utilizing a peak force tunneling atomic force microscope (PF-TUNA, FastScan Bio) under an applied bias of 8 V and a peak force of 5 nN.

2.3. Finite-element (FE) simulation

The finite-element simulations based on actual microstructural features were performed using the heat transfer module in COMSOL Multiphysics® to analyze the heat conduction behavior of the Al-xFe and Al-xNi alloys. The input parameters for the Al matrix and various secondary phases are listed in Table 3 and are treated as temperature-independent. The effective thermal conductivity (λ_{eff}) of each alloy system was calculated in accordance with Fourier's law.

3. Results

3.1. Microstructure

Fig. 2 depicts the solidification paths of the Al-Ni alloys and Al-Fe alloys with diverse alloying contents, computed by Pandat software based on the nonequilibrium equation of Scheil's model [37]. With the increment of the Ni contents, the liquidus temperature of Al-Ni alloys decreases (Fig. 2a). The solidification initiates with the formation of α -Al from the liquid phase, followed by a eutectic reaction ($L\rightarrow \alpha$ -Al + Al₃Ni)

Table 3The FE simulation parameters for the Al matrix and diverse secondary phases [26,34–36].

Materials	Density/ g·cm ⁻³	Specific heat capacity/ $J \cdot (g \cdot K)^{-1}$	Thermal conductivity/W $(m \cdot K)^{-1}$
Al matrix	2.70	0.900	238
Al ₃ Ni	4.06	0.169	35
$Al_{13}Fe_4$	3.99	0.040	15

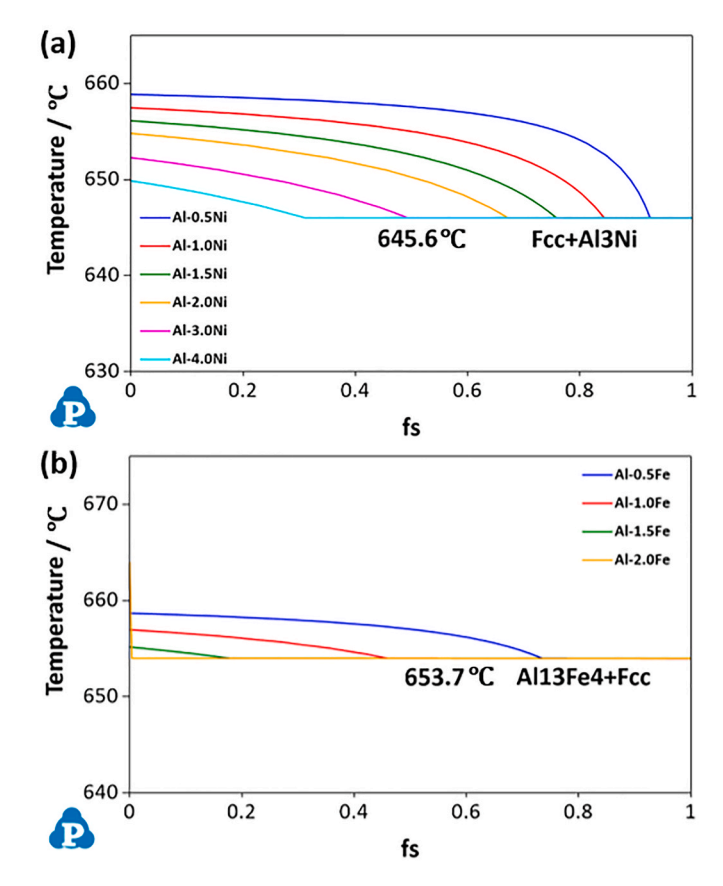


Fig. 2. Solidification paths of (a) Al-Ni alloys and (b) Al-Fe alloys with diverse alloying contents.

occurring at 645.6 °C. The eutectic fraction increased progressively with the Ni contents. Fig. 2b illustrates the solidification paths of the Al-Fe alloys. Correspondingly, the α -Al initially forms from liquid and the eutectic reaction (L \rightarrow α -Al + Al₁₃Fe₄) triggered at 653.7 °C. The eutectic fraction steadily increased with the Fe contents. Notably, the primary phase transitioned to Al₁₃Fe₄ (forming between 664.0 and 653.7 °C) when the Fe contents reached 2.0 wt %, which surpassed the Al-Fe eutectic point (1.83 wt%).

Fig. 3 depicts the microstructure of the Al-xNi alloys with varying Ni contents (x = 0.5, 1.0, 1.5, 2.0, 3.0, and 4.0 wt %). The microstructure of Al-0.5Ni alloy is primarily composed of the α -Al matrix and the eutectic structure (α -Al + eutectic Al-Ni secondary phases). Based on the XRD patterns presented in Fig. 5a, the eutectic Al-Ni secondary phase is identified as Al_3Ni. The area fractions of the eutectic structure in the Al-xNi alloys were estimated to be 10.2 %, 13.2 %, 16.5 %, 19.0 %, 30.3 %, and 35.0 %, respectively. This indicated a progressive increase in eutectic contents with increasing Ni concentration. The magnified images in Fig. 3 further reveal that the Al_3Ni within the lamellar eutectic structure presents a finely dispersed, rod-like morphology [38].

Fig. 4 illustrates the microstructure of the Al-xFe alloys with different Fe contents (x = 0.5, 1.0, 1.5, and 2.0 wt %). As depicted in Fig. 4a, the microstructural characteristics of the Al-0.5Fe alloys resemble those of the Al-0.5Ni alloys, which primarily consist of the α -Al matrix and the eutectic structure (α -Al + eutectic Al-Fe secondary phases). The eutectic Al-Fe secondary phase is demonstrated to be Al₁₃Fe₄ according to the XRD spectra shown in Fig. 5b. Meanwhile, the area fraction of the eutectic structure increased with the Fe contents, reaching approximately 14.8 %, 18.3 %, 23.9 %, and 27.0 % for Al alloys containing 0.5, 1.0, 1.5, and 2.0 wt % Fe, respectively. The inset micrographs in Fig. 4 exhibit that the eutectic structure adopts a characteristic lamellar morphology throughout the Al-Fe alloys [15]. Besides, the needle-like primary Al₁₃Fe₄ is observed when the concentration of Fe reaches 2.0 wt % (Fig. 4d) [30]. This morphological feature was regarded as a substantial impediment to electron mobility, consequently exacerbating the degradation of electrical conductivity [28].

Fig. 5 exhibits the XRD spectra of the Al-Ni and Al-Fe alloys with diverse alloying contents. For the representative Al-Ni alloys (Al-1.0, 2.0, and 4.0 wt % Ni) (Fig. 5a), the diffraction peaks corresponding to the α -Al matrix and the Al₃Ni secondary phase are clearly identified. Besides, the XRD patterns of the Al-Fe alloys (Fig. 5b) display peaks

attributable to the α -Al matrix and the Al $_1$ 3Fe $_4$ secondary phase. Notably, the intensities of the Al $_3$ Ni and Al $_1$ 3Fe $_4$ peaks increased with the Ni and Fe contents, respectively, which probably suggested a corresponding increase in the volume fractions of these secondary phases [39]. This deduction is consistent with the microstructural characteristics of the Al-Ni (Fig. 3) and Al-Fe alloys (Fig. 4) with different alloying contents.

3.2. Electrical/thermal conductivity

Fig. 6a illustrates the evolution of the electrical conductivity in Al-Ni and Al-Fe alloys with the diverse alloying contents. The Al-xNi alloys (x = 0.5, 1.0, 1.5, and 2.0) maintained outstanding electrical conductivity above 31.7 MS/m, highlighting their potential for high-conductivity applications. At identical alloying concentrations, the electrical conductivity of the Al-Ni alloys consistently exceeded that of the Al-Fe alloys. The electrical conductivity of both alloy systems exhibited a monotonic decline with increasing Ni or Fe content. Specifically, for the Al-Ni alloys, the least-squares fitting of the electrical conductivitycomposition curves revealed that the electrical conductivity decreased by approximately 1.3 MS/m per 1 wt % increase in Ni content. In contrast, the Al-Fe alloys exhibited a steeper decline, with electrical conductivity decreasing by approximately 2.9 MS/m per 1 wt % increase in Fe content. Fig. 6b presents the variation in the thermal conductivity of the diverse Al-Ni and Al-Fe alloys. Similarly, the thermal conductivity of the Al-Ni alloys consistently surpassed that of the Al-Fe alloys at equivalent alloying contents. Furthermore, the thermal conductivity exhibited a continuous decline with increasing Ni and Fe contents. This decreasing trend aligns with the corresponding variation in electrical conductivity (Fig. 6a), which is consistent with the Wiedemann-Franz law [22]. Quantitatively, the thermal conductivity of the Al-Ni alloys decreased by approximately 17.6 W/(m·K) per 1 wt % increase in Ni content, whereas that of the Al-Fe alloys declines by about 21.0 W/(m·K) per 1 wt % increase in Fe content. The differential effects of the Al-Ni and Al-Fe secondary phases on both electrical and thermal conductivity will be systematically discussed in Section 4.

3.3. Mechanical properties

Fig. 7a and c display the representative tensile stress-strain curves of

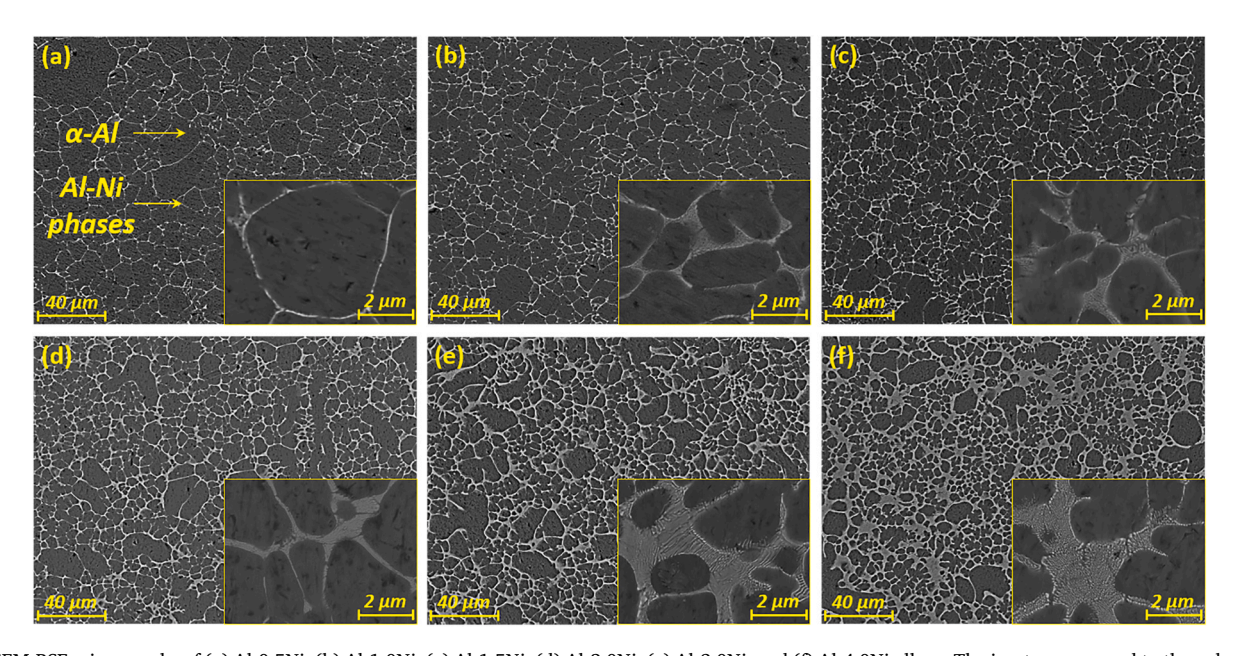


Fig. 3. SEM-BSE micrographs of (a) Al-0.5Ni, (b) Al-1.0Ni, (c) Al-1.5Ni, (d) Al-2.0Ni, (e) Al-3.0Ni, and (f) Al-4.0Ni alloys. The insets correspond to the enlarged view of the eutectic structure.

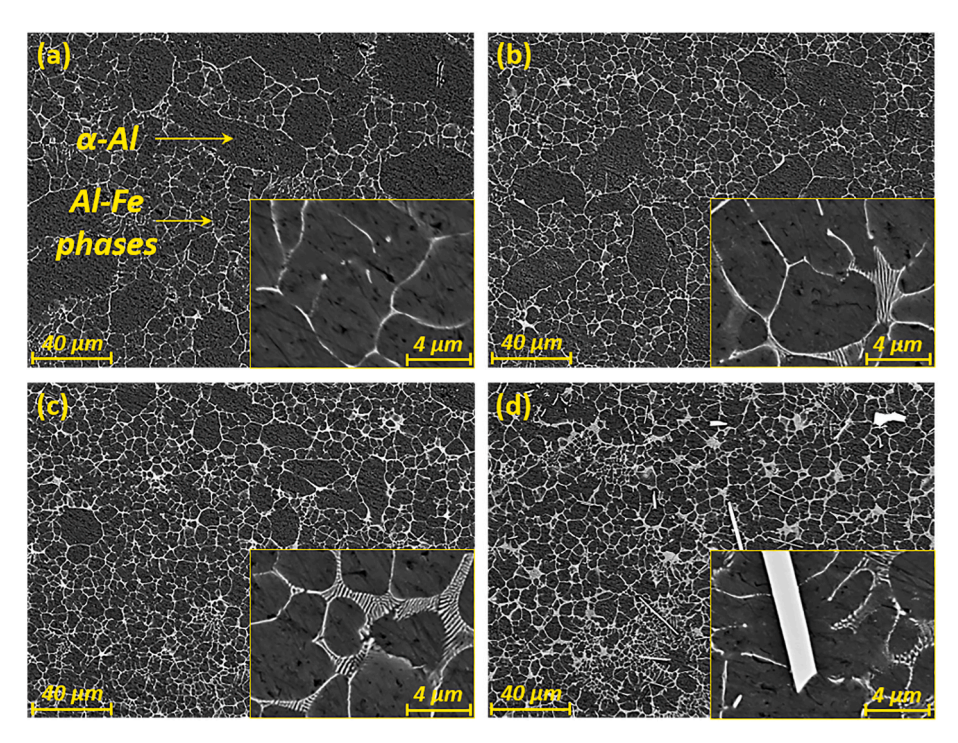


Fig. 4. SEM-BSE micrographs of (a) Al-0.5Fe, (b) Al-1.0Fe, (c) Al-1.5Fe, and (d) Al-2.0Fe alloys. The insets correspond to the enlarged view of the eutectic structure and the needle-like phase.

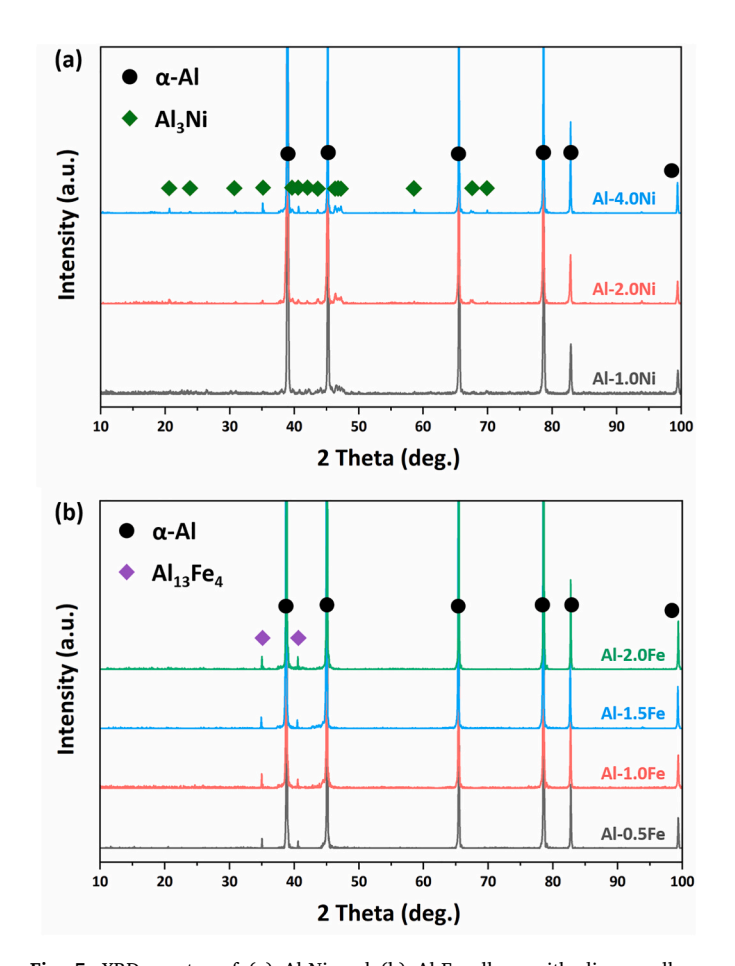


Fig. 5. XRD spectra of (a) Al-Ni and (b) Al-Fe alloys with diverse alloying contents.

the Al-Ni and Al-Fe alloys with varying alloying contents, respectively. Correspondingly, Fig. 7b and d summarize the evolution of mechanical properties for these two alloy systems. Both the yield strength (YS) and ultimate tensile strength (UTS) exhibited a consistent increase with rising alloying contents in the Al-Ni and Al-Fe alloys, while the elongation (EL) showed a gradual decreasing trend. As depicted in Table 4, the Al-xNi alloys (x = 1.5 and 2.0) exhibit favorable mechanical properties (UTS \geq 130 MPa) along with excellent electrical conductivity (σ > 31.7 MS/m) and thermal conductivity (λ > 193 W/(m·K)) (Fig. 6), indicating promising engineering applicability.

4. Discussion

4.1. Effect of secondary phases on electrical conductivity

The electrical conductivity of metals fundamentally originates from the directional motion of free electrons. The electron scattering in alloys exhibits characteristics of multiple dimensions and various sources, such as solute atoms, secondary phases, grain boundaries, and voids. Specifically, solute atoms are widely recognized as the primary scattering centers, as impurity atoms-induced lattice distortions contribute most significantly to the reduction in electrical conductivity of Al alloys [13]. Nevertheless, secondary phases, which often occupy a considerable volume fraction of Al alloys, can also exert a considerable influence on electrical conductivity degradation. To accurately assess the effect of secondary phases on the electrical conductivity of Al alloys, it was imperative to first eliminate or minimize the influence of solute atoms as a confounding variable. Table 5 summarizes the EDS point analysis of solute elements within the Al matrix at random locations. Given the low solid solubility limits of Ni (0.19 at. %) and Fe (0.02 at. %) in the Al matrix [25], the EDS results for various Al-Ni and Al-Fe alloys confirmed that Ni and Fe were virtually undetectable in the Al matrix [15,38]. This negligible solute content ensured that the variation in solute atom concentration was effectively minimized, thereby enabling a more reliable assessment of the influence of secondary phases on the electrical conductivity of Al alloys.

To enable a quantitative comparison of the microscopic electrical

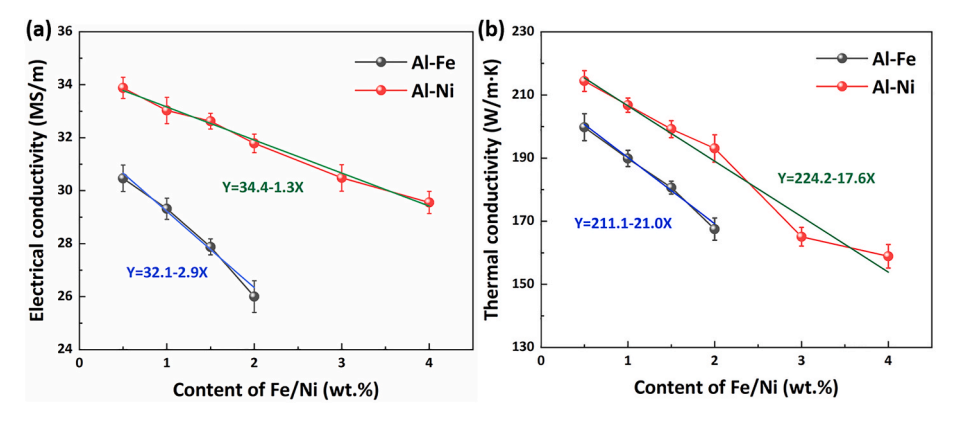


Fig. 6. (a) Electrical conductivity and (b) thermal conductivity of Al-Ni and Al-Fe alloys with diverse alloying contents.

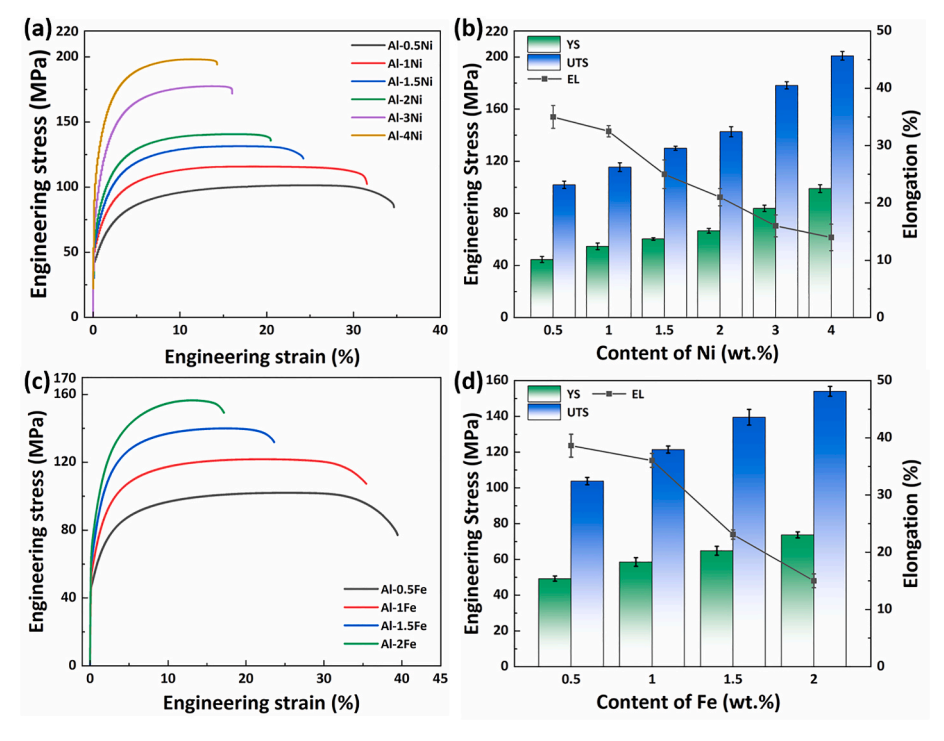


Fig. 7. Tensile stress-strain curves of (a) Al-Ni and (c) Al-Fe alloys with diverse alloying contents. Corresponding evolution of mechanical properties for (b) Al-Ni and (d) Al-Fe alloys as a function of alloying contents.

Table 4Mechanical properties of diverse Al-Ni and Al-Fe alloys.

Alloys	YS/ MPa	UTS/ MPa	EL/ %	Alloys	YS/ MPa	UTS/ MPa	EL/ %
Al- 0.5Ni	44.6	101.9	35.0	Al- 0.5Fe	49.3	103.8	38.6
Al- 1.0Ni	54.7	115.5	32.5	Al- 1.0Fe	58.6	121.5	36.1
Al- 1.5Ni	60.4	130.0	25.0	Al- 1.5Fe	64.9	140.0	23.1
Al- 2.0Ni	66.7	142.6	21.2	Al- 2.0Fe	73.7	154.0	15.0
Al- 3.0Ni	83.8	178.2	16.1				
Al- 4.0Ni	99.0	200.9	14.0				

Table 5EDS point analysis of the solute atoms within the Al matrix at random locations.

Alloys	Al/at. %	Ni/at. %	Alloys	Al/at. %	Fe/at. %
Al-0.5Ni	100	/	Al-0.5Fe	100	/
Al-1.0Ni	100	/	Al-1.0Fe	100	/
Al-1.5Ni	100	/	Al-1.5Fe	100	/
Al-2.0Ni	100	/	Al-2.0Fe	100	/
Al-3.0Ni	99.95	0.05			
Al-4.0Ni	99.91	0.09			

conductivity among different secondary phases, the microscopic electric conduction behavior of each secondary phase was scrutinized using the PF-TUNA technique [40]. Fig. 8a, c, and e show the surface topographies of eutectic Al $_3$ Ni, eutectic Al $_1$ 3Fe $_4$, and needle-like primary Al $_1$ 3Fe $_4$, respectively. The localized TUNA current-voltage (I-V) measurements at points 1, 2, and 3 exhibit TUNA current values of 0.68 nA (Fig. 8b), 0.58 nA (Fig. 8d), and 0.20 nA (Fig. 8f), respectively. The disparity in measured TUNA currents underscored the distinct microscopic electrical

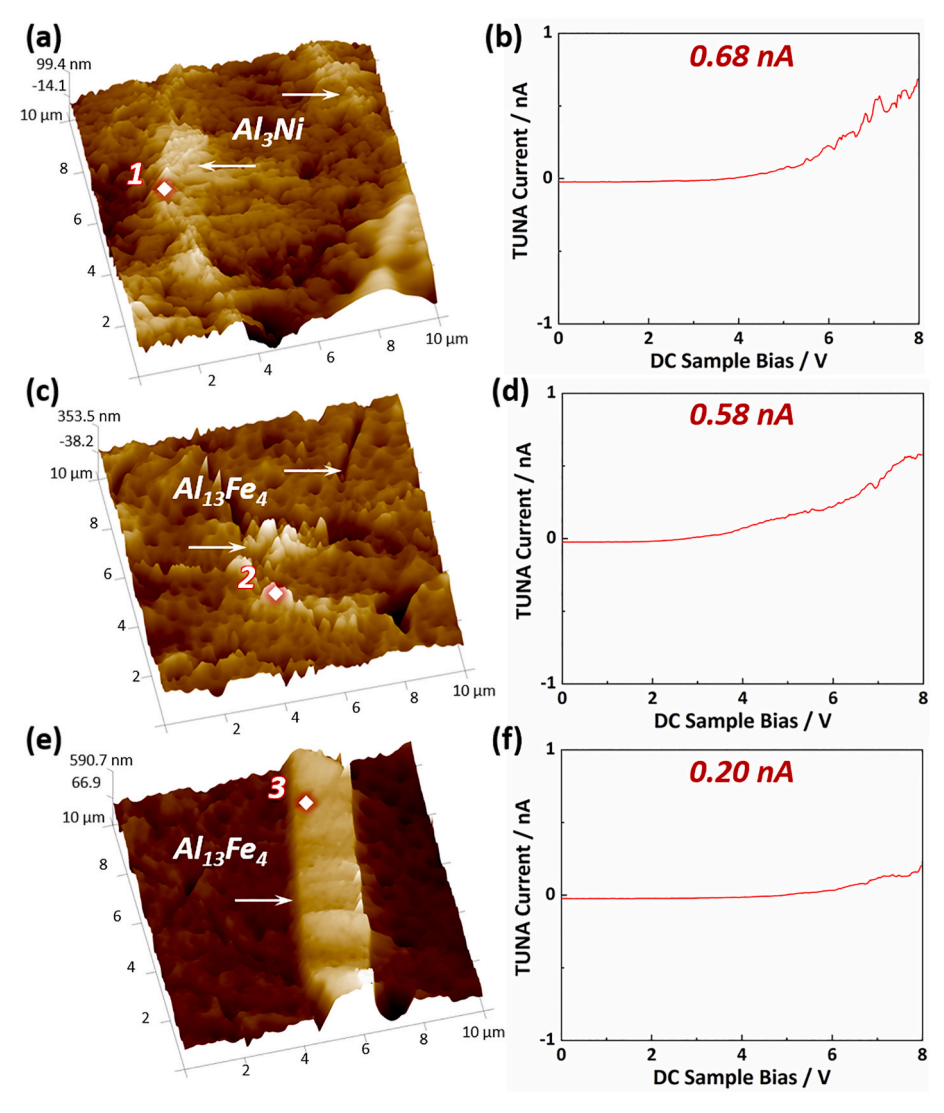


Fig. 8. AFM surface topographies and corresponding TUNA current-voltage curves of (a, b) eutectic Al_3Ni , (c, d) eutectic $Al_{13}Fe_4$, and (e, f) needle-like primary $Al_{13}Fe_4$.

conductivity of the diverse secondary phases, with elevated current levels signifying improved electron transport capability at the microscale. Thus, the microscopic electrical conductivity of the secondary phases followed the order: eutectic Al₃Ni > eutectic Al₁₃Fe₄ > needle-like Al₁₃Fe₄. The superior electrical conductivity of Al₃Ni compared to Al₁₃Fe₄ probably accounted for the less detrimental effect of Ni on the electrical conductivity of Al alloys (Fig. 6a). Furthermore, even within the same secondary phase composition, morphological variations can significantly impact the electrical conductivity of the Al alloys. Specifically, the needle-like Al₁₃Fe₄, with a higher aspect ratio, tends to impose more severe obstruction to free electron movement than that of the eutectic Al₁₃Fe₄, thereby further degrading electrical conductivity of Al alloys (Fig. 6a). In addition, an increased volume fraction of secondary phases (Figs. 3 and 4) intensifies electron scattering, exacerbating the deterioration of electrical conductivity (Fig. 6a). Therefore, the microscopic electrical conductivity, morphology, and volume fraction of secondary phases emerge as the key factors governing the electrical conductivity of Al alloys.

4.2. Effect of secondary phases on thermal conductivity

The influence of solute atoms on thermal conductivity is generally one order of magnitude greater than that of second phases [41]. This

pronounced effect is primarily attributed to the severe lattice distortion induced by solute atoms, which strongly impedes the transport of free electrons [42]. As shown in Table 5, the negligible solute concentration of Ni/Fe in the Al matrix effectively eliminates the influence of solute atoms, thereby enabling a focused investigation into the effect of secondary phases on thermal conductivity. Various heat conduction models and finite element (FE) simulations based on actual microstructural features were employed to quantitatively scrutinize the effect of Al_3Ni and $Al_{13}Fe_4$ on the thermal conductivity of Al alloys.

Multiple theoretical models of thermal conductivity were utilized to investigate the heat conduction behaviors and validate experimental

Table 6Theoretical models for predicting thermal conductivity [43–46].

Туре	Model	Theoretical equation
Continuous	Rayleigh	$rac{\lambda}{\lambda_m} = 1 + igg(rac{\lambda_s - \lambda_m}{\lambda_m}igg)V_s$
	Parallel	$\lambda = \frac{1}{\left[\left(V_m/\lambda_m\right) + \left(V_s/\lambda_s\right)\right]}$
Discontinuous	Maxwell	$\lambda = \lambda_m \left[rac{2\lambda_m + \lambda_s + 2V_s(\lambda_s - \lambda_m)}{2\lambda_m + \lambda_s - V_s(\lambda_s - \lambda_m)} ight]$
	EMT	$V_m rac{\lambda_m - \lambda}{\lambda_m + 2\lambda} + V_s rac{\lambda_s - \lambda}{\lambda_s + 2\lambda} = 0$

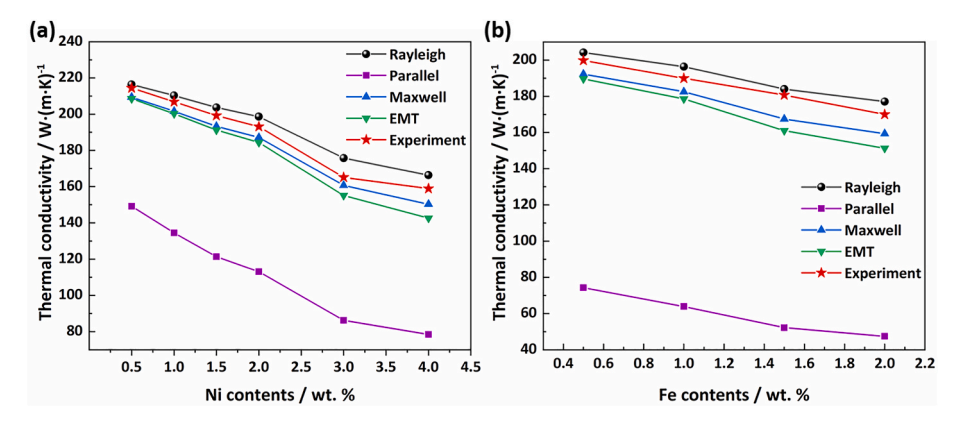


Fig. 9. Comparative analysis of the experimental and the theoretical thermal conductivity of (a) Al-Ni alloys and (b) Al-Fe alloys with diverse alloying contents.

results. Table 6 summarizes the theoretical models employed to predict the thermal conductivity of various Al-Ni and Al-Fe alloys. Fig. 9a and b displays a quantitative comparison between the predicted values and the experimental measurements. The thermal conductivity of both the Al-Ni and Al-Fe alloys exhibited the best overall agreement with the Rayleigh model for the continuous secondary phase, which was consistent with the observed morphologies of Al $_3$ Ni and Al $_3$ Fe $_4$ shown in Figs. 3 and 4. Furthermore, the experimental thermal conductivity was lower than the theoretical predictions. This discrepancy can be attributed to the Rayleigh model's omission of electron scattering mechanisms such as grain boundaries.

Where λ , λ_m , and λ_s represent the thermal conductivity of the Al alloys, α -Al matrix, and secondary phases, respectively. V_s and V_m are the volume fraction of the secondary phases and α -Al matrix, respectively.

FE simulations based on actual microstructure were conducted to quantitatively scrutinize secondary phase type, morphology, and volume fraction on the thermal conductivity of the Al alloys. Four representative alloying contents (Al-0.5Ni, Al-2.0Ni, Al-0.5Fe, and Al-2.0Fe alloys) characterized by distinct secondary phase thermal conductivity and volume fractions were employed to investigate the heat conduction behavior influenced by the secondary phases. The actual microstructural features of the Al-Ni and Al-Fe alloys (insets in Figs. 3a, d and 4a, d) were

implemented in the FE simulations for the quantitative evaluation. The constant temperature difference was maintained in 373 K at the left side and 298 K at the right side. The top and bottom surfaces were treated as thermally insulated to minimize heat loss to the environment, thereby isolating the conductive behavior through the material microstructure. As illustrated in Fig. 10a, the heat flux is predominantly conducted through the Al matrix due to its intrinsically superior thermal conductivity, whereas a significant reduction in heat flux occurs within the Al₃Ni secondary phases with comparatively lower thermal conductivity. Correspondingly, a notable concentration of heat flux appeared at the border between the Al matrix and the secondary phases. With an increasing volume fraction of Al₃Ni, the obstruction to heat conduction was progressively intensified (Fig. 10b). A similar reduction in heat flux is revealed in the Al-0.5Fe alloy (Fig. 10c), where the Al₁₃Fe₄ secondary phases exhibit analogous obstruction to heat conduction. Furthermore, this inhibition was exacerbated by the high aspect ratio of the needlelike Al₁₃Fe₄ phases (Fig. 10d), which further intensified electron scattering and impeded heat conduction. Based on Fourier's law, the effective thermal conductivity of the Al-0.5Ni, Al-2.0Ni, Al-0.5Fe, and Al-2.0Fe alloys was 216.0, 200.9, 207.6, and 133.1 W/(m·K), respectively, which were consistent with the order of the experimental thermal conductivity. The effective thermal conductivity of the Al-Ni alloys was

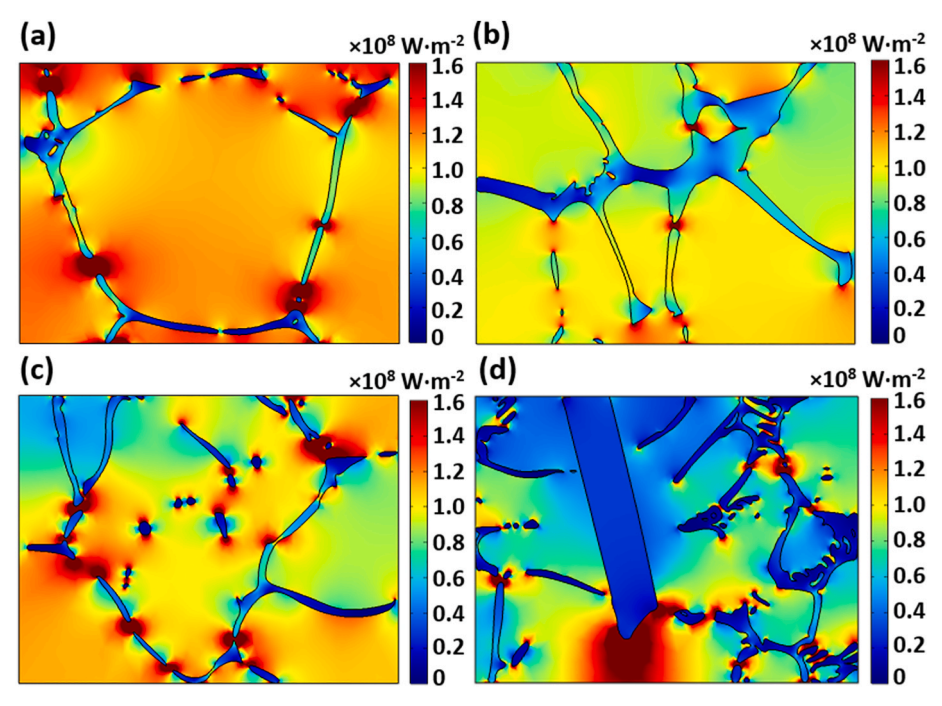


Fig. 10. FE simulations to the contour plot of the heat flux density in (a) Al-0.5Ni, (b) Al-2.0Ni, (c) Al-0.5Fe, and (d) Al-2.0Fe alloys, respectively.

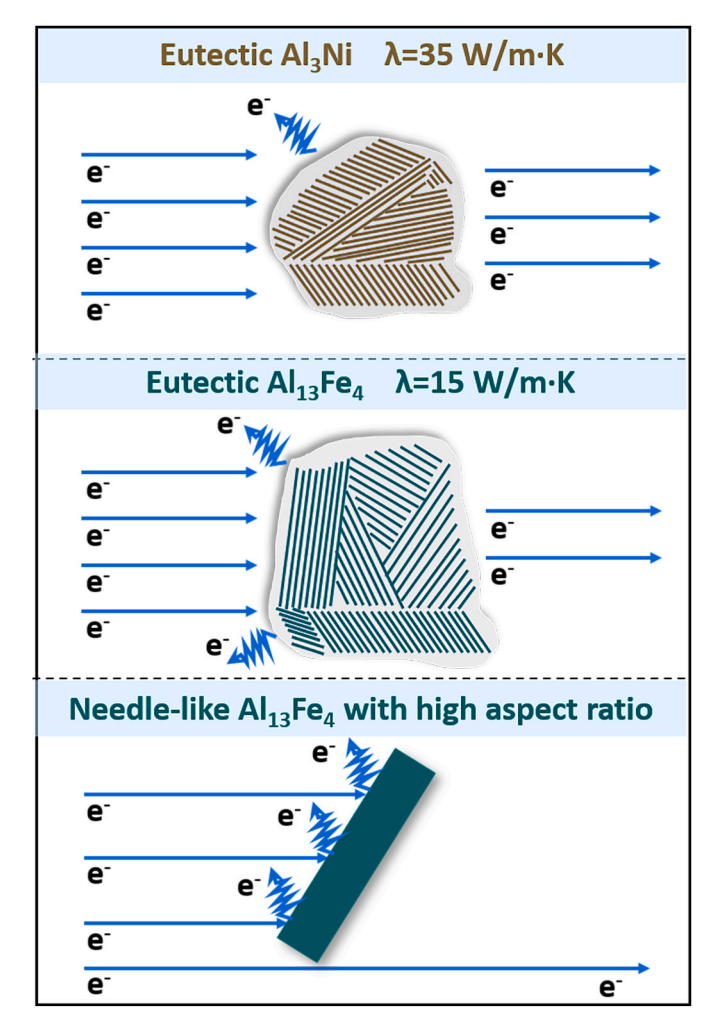


Fig. 11. Schematic diagram of the electric/heat conduction mechanism for distinct types and morphologies of secondary phases.

invariably higher than that of the Al-Fe alloys at equivalent alloying contents. This disparity can be primarily attributed to three key factors: First, the intrinsic thermal conductivity of Al₃Ni was higher than that of Al₁₃Fe₄, as summarized in Table 3. Second, the Al₁₃Fe₄ secondary phases exhibited a needle-like morphology with a high aspect ratio (the inset in Fig. 4d), which confined the pathways for free electron movement and intensified the electron scattering. Third, the volume fraction of the secondary phases in the Al-Fe alloys was greater than that in the Al-Ni alloys under the same alloying contents (Figs. 3 and 4), consequently providing a greater number of electron scattering sites. Consequently, at identical alloying contents, Al-Ni alloys exhibited superior thermal conductivity compared with that of the Al-Fe alloys. Collectively, the theoretical heat conduction models and FE simulations theoretically demonstrated that the intrinsic thermal conductivity, morphology, and volume fraction of secondary phases were the predominant factors influencing the thermal conductivity of Al alloys.

For alloys with the same alloying element (e.g., Al-Ni alloys), the volume fraction of Al_3Ni increases with the Ni contents (Fig. 3). Accordingly, the higher volume fraction of Al_3Ni intensifies electron scattering and reduces the available pathways for free electron transport [16], resulting in decreased electrical and thermal conductivity of the alloys (Fig. 6). For alloys with different alloying elements (e.g., Al-2.0Ni and Al-2.0Fe alloys), Al_{13} Fe $_4$ induces a more pronounced deterioration in electrical and thermal conductivity than Al_3Ni (Fig. 6) under the condition where the influence of solute atoms is negligible (Table 5). A schematic (Fig. 11) has been utilized to illustrate the underlying mechanism of electrical and heat conduction behaviors influenced by

different types and morphologies of secondary phases, which can be attributed to the following three factors. First, ${\rm Al_{13}Fe_4}$ exhibits inferior electric conduction properties (Fig. 8) and inherently lower thermal conductivity compared to ${\rm Al_3Ni}$ (Table 3). Second, the needle-like primary ${\rm Al_{13}Fe_4}$ is formed at an Fe content of 2.0 wt %, (the inset in Fig. 4d), which imposes stronger obstruction and scattering effects on electrons due to its high aspect ratio. Third, ${\rm Al_{13}Fe_4}$ exhibits a higher volume fraction at the identical alloying content (Figs. 3 and 4), thereby providing a greater number of electron scattering sites and increasing the probability of electron scattering. Provided that other service performance requirements are met, it can thus be reasonably speculated that secondary phases with superior microscopic conductive properties, finer morphologies, and lower volume fractions are more favorable for optimizing the electrical conductivity and thermal conductivity of Al alloys.

5. Conclusions

In summary, the HPDC Al-Ni and Al-Fe alloys with varying alloying contents were fabricated to investigate the influence of microscopic secondary phases on the macroscopic electrical and thermal conductivity of Al alloys. The main conclusions of this research can be drawn as follows:

- (1) The electrical and thermal conductivity of the Al-Ni alloys were invariably higher than those of the Al-Fe alloys at equivalent alloying contents.
- (2) The electrical conductivity of Al-Ni alloys decreased at a rate of approximately 1.3 MS/m per 1 wt% Ni addition, while that of Al-Fe alloys declined more rapidly at ~2.9 MS/m per 1 wt% Fe. The thermal conductivity of Al-Ni alloys decreased by approximately 17.6 W/(m⋅K) per 1 wt% Ni, whereas that of Al-Fe alloys exhibited a steeper decline of ~21.0 W/(m⋅K) per 1 wt% Fe.
- (3) The enhanced electrical and thermal conductivity of Al-Ni alloys can be primarily attributed to the intrinsically superior microscopic electrical and thermal conductivity of Al₃Ni, the elimination of morphology-induced electron scattering from needle-like Al₁₃Fe₄, and the comparatively lower volume fraction of Al₃Ni.
- (4) Both the YS and UTS exhibited a consistent increase with rising alloying contents in the Al-Ni and Al-Fe alloys, while the elongation showed a gradual decreasing trend. The Al-xNi alloys (x = 1.5 and 2.0) exhibited considerable mechanical properties (UTS≥130 MPa) along with remarkable electrical conductivity (σ > 31.7 MS/m) and thermal conductivity (λ > 193 W/(m·K)), underscoring strong potential for engineering applications.

Declaration of competing interest

The authors declare that they have no known competing financial interests or personal relationships that could have appeared to influence the work reported in this paper.

Acknowledgments

This work was supported by the National Natural Science Foundation of China [projects No. 52271009, 52301059], the Science and Technology Plan Project of Yunnan Province [No. 202502AB080005], the Xiaoqin Zeng Expert Workstation in Yunnan Province [No. 202505AF350043], the Young Elite Scientists Sponsorship Program by the China Association for Science and Technology (CAST) [No.2024QNRC001].

References

[1] Gao YC, Dong BX, Yang HY, Yao XY, Shu SL, Kang J, Meng J, Luo CJ, Wang CG, Cao K, Qiao J, Zhu M, Qiu F, Jiang QC. Research progress, application and

- development of high performance 6000 series aluminum alloys for new energy vehicles. J Mater Res Technol 2024;32:1868–900. https://doi.org/10.1016/j.imrt.2024.08.018.
- [2] Li Y, Hu A, Fu Y, Liu S, Shen W, Hu H, Nie X. Al alloys and casting processes for induction motor applications in battery-powered electric vehicles: a review. Metals 2022;12. https://doi.org/10.3390/met12020216.
- [3] Trudonoshyn O, Rehm S, Randelzhofer P. Körner, Improvement of the highpressure die casting alloy Al-5.7Mg-2.6Si-0.7Mn with Zn addition. Mater Char 2019;158:109959. https://doi.org/10.1016/j.matchar.2019.109959.
- [4] Zhang D, Li D, Ren L, Zhao K, Zhao Z, Yan X, Liu G, Cha W, Liu S, Liu X. A new synergy to overcome the strength-ductility trade-off dilemma in Al–Si–Cu alloy by micro-nano-particle complex clusters. Mater Des 2023;230:111973. https://doi. org/10.1016/j.matdes.2023.111973.
- [5] Feyer F, Weigand M, Randelzhofer P, Körner C. Increasing the conductivity of aluminium high-pressure die casting alloy AlSi9Cu3Fe (226D) by Sr modification of eutectic and intermetallic phases. Mater Sci Eng B 2025;316:118109. https:// doi.org/10.1016/j.mseb.2025.118109.
- [6] Villanueva E, Vicario I, Crespo I, Guraya T, Hurtado I, Albizuri J. Development of a new ductile heat-treated multi-component aluminium by HPDC with highperformance properties for temperature applications. J Alloys Compd 2025;1020. https://doi.org/10.1016/j.jallcom.2025.179146.
- [7] Dong Q, Zhang Y, Wang J, Huang L, Nagaumi H. Enhanced strength-conductivity trade-off in Al-Mg-Si alloys with optimized Mg/Si ratio. J Alloys Compd 2024;970: 172682. https://doi.org/10.1016/j.jallcom.2023.172682.
- [8] Huang Y, Liu Y, Xiao Z, Huang Y. A trade-off between mechanical strength and electrical conductivity of Al–Zn–Mg–Cu alloy via Ag alloying and retrogression reaging heat treatment. Mater Sci Eng 2023;880:145230. https://doi.org/10.1016/j. ppeg 2023 14530.
- [9] Hou JP, Li R, Wang Q, Yu HY, Zhang ZJ, Chen QY, Ma H, Wu XM, Li XW, Zhang ZF. Breaking the trade-off relation of strength and electrical conductivity in pure Al wire by controlling texture and grain boundary. J Alloys Compd 2018;769:96–109. https://doi.org/10.1016/j.jallcom.2018.07.358.
- [10] Zhu R, Chen W, Chen Z, Sui Y, Qu Y. Effect of combined addition of Ni and Sc on microstructure and high-temperature mechanical properties of an Al-Cu-Mn alloy. J Alloys Compd 2025;1023:179971. https://doi.org/10.1016/j. iallcom.2025.179071
- [11] Li R, Takata N, Suzuki A, Kobashi M. Design of heat-resistant Al-Mg –Zn–Cu–Ni quinary alloy: controlling intermetallic phases and mechanical performance at elevated temperature. Mater Sci Eng 2022;857:144055. https://doi.org/10.1016/j.msea.2022.144055
- [12] Wang M, Wu J, Yang S, Knezevic M, Huang Z, Zhao Y, Liu T, Shen B, Wang J. Processing of an as-cast Al-7.5 wt%Y eutectic alloy by rolling and annealing to improve the tradeoff between strength and electrical conductivity. Mater Sci Eng 2024:890. https://doi.org/10.1016/j.msea.2023.145950.
- [13] Wang Y, Zhu L, Niu G, Mao J. Conductive Al alloys: the contradiction between strength and electrical conductivity. Adv Eng Mater 2021;23:1–22. https://doi. org/10.1002/adem.202001249.
- [14] Wang W, Pan Q, Jiang F, Yu Y, Lin G, Wang X, Ye J, Pan D, Huang Z, Xiang S, Li J, Liu B. Microstructure evolution and performances of Al-0.7Mg-0.6Si-0.2Ce-X (X [dbnd]Sc, Y and Zr) alloys with high strength and high electrical conductivity. J Alloys Compd 2022:895 https://doi.org/10.1016/j.iallcom.2021.65654
- J Alloys Compd 2022;895. https://doi.org/10.1016/j.jallcom.2021.162654.

 [15] Xu R, Lu Y, Dai Y, Debastiani R, Hahn H, Ivanisenko Y. Simultaneous improvement of mechanical strength and electrical conductivity in Al-2.5 wt% Fe alloy rods with high thermal stability by high-pressure torsion extrusion. Mater Char 2025;224. https://doi.org/10.1016/j.matchar.2025.114956.
- [16] Zhang Y, Luo X, Zhu L, Chen Y, Luo Q, Xu J, Lu Q. Design of non-heat-treatable Al-Fe-Ni alloys with high electrical conductivity and high strength via CALPHAD approach. J Alloys Compd 2024;1009. https://doi.org/10.1016/j.
- [17] Xu S, Lin B, Jiang Y, He X, Fan Z, Xiao H, Fu Z. Simultaneously improving mechanical properties and electrical conductivity of Al-1.9Mn alloys with different Mg and Si addition. J Alloys Compd 2024;999:175072. https://doi.org/10.1016/j. iallcom.2024.175072.
- [18] Cui X, Ye H, Liu H, Li X, Man Q, Li H, Cui H, Feng R, Pan Y. The improvement mechanism of good matching between electrical conductivity and mechanical properties for Al-4Si-0.8Mg-0.6Fe alloy. J Alloys Compd 2023;938:168275. https://doi.org/10.1016/j.jallcom.2022.168275.
- [19] Dong Q, Wang R, Wang J, Nagaumi H. Influence of Mg/Si ratio on the mechanical strength and electrical conductivity of Al-Mg-Si alloys. Mater Today Commun 2025;42:111439. https://doi.org/10.1016/j.mtcomm.2024.111439.
- [20] Lunn KF, Apelian D. Thermal and Electrical Conductivity of Aluminum Alloys: fundamentals, structure-property relationships, and pathways to enhance conductivity. Mater Sci Eng 2025;924:147766. https://doi.org/10.1016/j. msea 2024.147766
- [21] Yao F, Li Z, Hu B, Jiang Z, Zeng X, Li D. Unveiling the interface between second phases and matrix on thermal conductivity of Mg alloys. J Mater Res Technol 2024; 28:1824–33. https://doi.org/10.1016/j.jmrt.2023.12.116.
- [22] Zhou D, Li L, Zhao K, Yang W, Kang H, Guo E, Li J, Zhang T, Chen Z, Wang T. Comprehensive regulation of mechanical properties and thermal conductivity of Al-Si-Fe alloys through the mixed-additive (Sr and TiB2) strategy. J Alloys Compd 2024;1005:175850. https://doi.org/10.1016/j.jallcom.2024.175850.
- [23] Murashkin MY, Sadykov DI, Mavlyutov AM, Kazykhanov VU, Enikeev NA. Effect of Mg content on mechanical properties and electrical conductivity of ultrafinegrained Al-Mg-Zr wires produced by ECAP-Conform and drawing. J Mater Sci 2024;59:5923–43. https://doi.org/10.1007/s10853-024-09402-0.

- [24] Ghiaasiaan R, Amirkhiz BS, Shankar S. Quantitative metallography of precipitating and secondary phases after strengthening treatment of net shaped casting of Al-Zn-Mg-Cu (7000) alloys. Mater Sci Eng 2017;698:206–17. https://doi.org/10.1016/j. msea 2017.05.047
- [25] Liu Y, Liu Y, Akhtar S, Wang P, He Z, Jiao X, Ge S, Yuan G, Zhang Y, Li X, Xiong S. Thermal conductivity of binary Al alloys with different alloying elements. J Alloys Compd 2025;1010:177257. https://doi.org/10.1016/j.jallcom.2024.177257.
- [26] Chen JK, Hung HY, Wang CF, Tang NK. Thermal and electrical conductivity in Al-Si/Cu/Fe/Mg binary and ternary Al alloys. J Mater Sci 2015;50:5630–9. https://doi.org/10.1007/s10853-015-9115-9.
- [27] Qi M, Kang Y, Xu Y, Wulabieke Z, Li J. A novel rheological high pressure diecasting process for preparing large thin-walled Al-Si-Fe-Mg-Sr alloy with high heat conductivity, high plasticity and medium strength. Mater Sci Eng 2020;776. https://doi.org/10.1016/j.msea.2020.139040.
- [28] Li N, Ge F, Wu S, Tan H, Hu Z. Effect of La-Ce additions on microstructure and mechanical properties of cast Al-3Si-0.5Cu-0.7Fe alloy with high thermal conductivity. J Alloys Compd 2025;1024:180249. https://doi.org/10.1016/j. iallcom.2025.180249
- [29] Li C, Hou H, Liu L, Huang C, Ren Y, Du J, Yin C. Effect of Sr modification on the microstructures, mechanical properties, and thermal conductivity of hypoeutectic Al-13.6Cu-6Si alloys. J Mater Eng Perform 2024. https://doi.org/10.1007/s11665-024.09752-5
- [30] Luo G, Zhou X, bo Li C, Du J, hua Huang Z. Design and preparation of Al-Fe-Ce ternary aluminum alloys with high thermal conductivity. Trans Nonferrous Metals Soc China 2022:1781–94. https://doi.org/10.1016/S1003-6326(22)65908-9 (English Ed. 32.
- [31] dos Santos SL, Antunes RA, Santos SF. Influence of injection temperature and pressure on the microstructure, mechanical and corrosion properties of a AlSiCu alloy processed by HPDC. Mater Des 2015;88:1071–81. https://doi.org/10.1016/j. matdes.2015.09.095.
- [32] Peng GS, Fu XY, Gu YC, Song GS, Chen SS, Sun QQ, Hua WD. Microstructural evolution and strengthening behavior of high-pressure die-cast High-Cu al-si-cu-mg alloy with T5 treatment. J Mater Eng Perform 2022;31:5432–40. https://doi.org/ 10.1007/s11665-022-06640-8.
- [33] Liu Y, Zhang Y, Liu W, Jiao X, Nishat H, Ajavavarakula D, Chen H, Xiong S. Enhanced mechanical properties and thermal conductivity of high-pressure diecast AlMg6Si2MnZr alloy by controlling the externally solidified crystals. J Mater Process Technol 2022;306:117645. https://doi.org/10.1016/j. imatprotec.2022.117645.
- [34] Terada Y, Ohkubo K, Mohri T, Suzuki T. Thermal conductivity of intermetallic compounds with metallic bonding. Mater Trans 2002;43:3167–76. https://doi.org/ 10.2320/matertrans.43.3167.
- [35] Chen HL, Doernberg E, Svoboda P, Schmid-Fetzer R. Thermodynamics of the Al3Ni phase and revision of the Al-Ni system. Thermochim Acta 2011;512:189–95. https://doi.org/10.1016/j.tca.2010.10.005.
- [36] Rank M, Gotcu P, Franke P, Seifert HJ. Thermodynamic investigations in the Al-Fe system: heat capacity measurements of three intermetallic phases. Intermetallics 2018;94:73–82. https://doi.org/10.1016/j.intermet.2017.12.015.
- [37] Hu B, Li Z, Li D, Ying T, Zeng X, Ding W. A hot tearing criterion based on solidification microstructure in cast alloys. J Mater Sci Technol 2022;105:68–80. https://doi.org/10.1016/j.jmst.2021.06.071.
- [38] Amigó A, Afonso CRM, Amigó V. Effect of Fe addition on microstructure and properties of powder metallurgy Ti35Nb10Ta alloy. Mater Sci Forum 2017;899 (MSF):206–11. https://dx.doi.org/10.4028/www.scientific.net/MSF.899.206.
- [39] Yao F, You G, Zeng S, Zhou K, Peng L, Ming Y. Fabrication, microstructure, and thermal conductivity of multilayered Cu mesh/AZ31 Mg foil composites. J Mater Res Technol 2021;14:1539–50. https://doi.org/10.1016/j.jmrt.2021.07.042.
 [40] Yao F, Hu B, Li Z, Li L, Han J, Jiang Z, Li D, Zeng X. Neuron-inspired structure
- [40] Yao F, Hu B, Li Z, Li L, Han J, Jiang Z, Li D, Zeng X. Neuron-inspired structure towards ultra-high thermal conductivity of Mg-based materials. Composites Part B 2025;297. https://doi.org/10.1016/j.compositesb.2025.112345.
- [41] Su C, Li D, Luo AA, Ying T, Zeng X. Effect of solute atoms and second phases on the thermal conductivity of Mg-RE alloys: a quantitative study. J Alloys Compd 2018; 747:431–7. https://doi.org/10.1016/j.jallcom.2018.03.070.
- [42] Liu Y, Akhtar S, Liu Y, Wan A, Wang P, Jiao X, Ge S, Yuan G, Zhang Y, Li X, Xiong S. The variation in microstructure and thermal conductivity of a plate-like Al-Fe-Ni high-pressure die casting. Mater Today Commun 2025;42:111132. https://doi.org/10.1016/j.mtcomm.2024.111132.
- [43] Yin WL, Dai J, Li YH, Li K. Electronic structures, elastic properties and debye temperature of the intermetallics in Mg-Zn-RE (RE=Ce, La)-Zr alloy: a firstprinciples calculation. Mater Today Commun 2021;29:1–10. https://doi.org/ 10.1016/j.mtcomm.2021.102891.
- [44] Newcomb BA, Giannuzzi LA, Lyons KM, Gulgunje PV, Gupta K, Liu Y, Kamath M, McDonald K, Moon J, Feng B, Peterson GP, Chae HG, Kumar S. High resolution transmission electron microscopy study on polyacrylonitrile/carbon nanotube based carbon fibers and the effect of structure development on the thermal and electrical conductivities. Carbon N Y 2015;93:502–14. https://doi.org/10.1016/j.carbon.2015.05.037.
- [45] Su C, Li D, Luo AA, Ying T, Zeng X. Effect of solute atoms and second phases on the thermal conductivity of Mg-RE alloys: a quantitative study. J Alloys Compd 2018; 747:431–7. https://doi.org/10.1016/j.jallcom.2018.03.070.
- [46] Li Z, Yao F, Hu B, Zhang W, Wang X, Han J, Zhou L, Jiang Z, Zeng X, Li D. Effect of thickness-dependent sandwich microstructure on the thermal conductivity of HPDC Mg-4Sm-2Al alloy. Metall Mater Trans A Phys Metall Mater Sci 2024;55: 1418-34. https://doi.org/10.1007/s11661-024-07326-7.